Correlated Electrical and Chemical Nanoscale Properties in Potassium-Passivated, Triple-Cation Perovskite Solar Cells

*Elizabeth M. Tennyson, Mojtaba Abdi-Jalebi, Kangyu Ji, Joseph L. Garrett, Chen Gong, Alison A. Pawlicki, Olga S. Ovchinnikova, Jeremy N. Munday, Samuel D. Stranks, Marina S. Leite**

Dr. Elizabeth M. Tennyson, Dr. Chen Gong, Prof. Marina S. Leite
Department of Materials Science and Engineering, University of Maryland, College Park, MD 20742, USA

Dr. Elizabeth M. Tennyson, Dr. Joseph L. Garret, Dr. Chen Gong, Prof. Jeremy N. Munday, Prof. Marina S. Leite
Institute for Research in Electronics and Applied Physics, University of Maryland, College Park, MD 20742, USA

Dr. Elizabeth M. Tennyson, Dr Mojtaba, Abdi-Jalebi, Kangyu Ji, Dr. Samuel D. Stranks
Cavendish Laboratory, University of Cambridge, JJ Thomson Avenue, CB3 0HE Cambridge, UK

Dr. Mojtaba Abdi-Jalebi
Institute for Materials Discovery, University College London, Torrington
Place, London WC1E 7JE, UK

Dr. Alison A. Pawlicki, Dr. Olga S. Ovchinnikova
Center for Nanophase Materials Sciences, Oak Ridge National Laboratory, Oak Ridge, TN 37831, USA

Prof Jeremy N. Munday
Department of Electrical and Computer Engineering, University of Maryland, College Park, MD, 20742, USA
Department of Electrical and Computer Engineering, University of California, Davis, CA, 95616, USA

Prof Marina S. Leite
Department of Materials Science and Engineering, University of California, Davis, CA, 95616, USA
E-mail: mleite@ucdavis.edu

Keywords: halide perovskites, solar cells, nanoscale, correlative microscopy, passivation

ABSTRACT Perovskite semiconductors are an exciting class of materials due to their promising performance outputs in optoelectronic devices. To boost their efficiency further, researchers introduce additives during sample synthesis, such as KI. However, it is not well understood how KI changes the material and, often, leaves precipitants. To fully resolve the role of KI, a multiple microscopy techniques is applied and the electrical and chemical behavior of a Reference (untreated) and a KI-treated perovskite are compared. Upon correlation between electrical and chemical nanoimaging techniques, we discover that these local properties are linked to the macroscopic voltage enhancement of the KI-treated perovskite. The heterogeneity revealed in both the local electrical and chemical responses indicates that the additive partially migrates to the surface, yet surprisingly; does not deteriorate the performance locally, rather, the voltage response homogeneously increases. The research presented within provides a diagnostic methodology, which connects the nanoscale electrical and chemical properties of materials, relevant to other perovskites, including multi-cation and Pb-free alternatives.

Introduction

Halide perovskite semiconductors are complex and promising materials to the optoelectronic research community, because they offer a low-cost solution for a wide variety of applications[1] and they exhibit excellent performance in photovoltaic (PV) devices despite demonstrating performance heterogeneity at the nanoscale.[2] Yet, prior to deployment into the PV market, various questions about the unique electrical, thermal, and structural instabilities must be resolved.[3] Thus far, the most stable perovskite materials that maintain a power conversion efficiency (η) > 20% incorporate a triple cation (Cs, FA = formamidinium, $CH_3(NH_2)_2^+$, and MA = methylammonium, $CH_3NH_3^+$) in the A-site of the perovskite ABX_3 structure, Pb^{2+} in the B-site, and a mixture of halides in the X-site (typically I or Br). Despite the effort that has gone into tailoring the possible compositions and into engineering the interfaces between the active layers,[4] a further increase in performance stability is required for a viable solar cell device.[5]

To address the stability challenge, scientists and engineers have recently focused on investigating defect passivation approaches, i.e. introducing small amounts of an additional species into the perovskite material either pre-, during, or post-synthesis in order to reduce the impact of surface defects.[6] For example, including excess amounts of PbI_2 during perovskite formation enhances the device performance by slowing the rate of charge carrier recombination at the interfaces between the perovskite and charge selective contacts and reducing the halide vacancy concentration.[7] Coating perovskites with quaternary ammonium halides (structure: $NR_4^+X^-$, where R=alkyl or aryl group, and X=halide) has shown prolonged charge carrier lifetimes, which increases the overall open-circuit voltage (V_{oc}) of the solar cell while also extending device stability to >800 hours in ambient conditions.[8] Additionally, by including a potassium-halide solution into the perovskite precursor, the resulting film's interfaces and grain boundaries become passivated, reducing *J-V* curve hysteresis and extending the solar cell's shelf life.[6b] Yet, this latter treatment route has also found that undesirable by-products are

formed,[9] even when the samples are only ever stored in a glove box environment (i.e. never exposed to ambient conditions, see also Figure S1 of supporting information).[10]

Several passivation techniques[11] have led to enhanced macroscopic PV performance, yet, there is little direct evidence for *how* (i) the additional chemical species are distributed within the solar cell device or (ii) the resulting local electrical and chemical properties interact and influence one another. Thus, there is a need for correlative studies to link multiple nanoscale material properties.[2a, 3f, 12] In this work we use the terminology correlation to establish the effect of one material property (e.g. chemical) on another (such as electrical). For example, recently, peak force infrared microscopy was implemented to relate local mechanical and chemical properties of a variety of materials, including perovskite crystals.[13] Here, a link between perovskite surface degradation and a reduction in the mechanical modulus was found. Kong et al., implemented photoinduced force microscopy in conjunction with conductive atomic force microscopy (c-AFM) to study the structure-function relationship between two electronically distinct polymers.[14] They found that the semiconducting polymer is embedded within the insulating polymer's aggregates. Further, our prior work implementing time-of-flight secondary ion mass spectroscopy (ToF-SIMS) in conjunction with Kelvin probe force microscopy (KPFM) connected the perovskite chemical composition with the short and long-term voltage response in multiple halide perovskite films.[3d] Employing such techniques to provide a more in-depth understanding of how perovskite passivation techniques boost device performance at the nanoscale will be necessary to rationally fabricate the next-generation of halide perovskite solar cells.

Here we present a fully experimental correlative microscopy methodology that details the intricate relationship between the electrical and chemical properties of triple cation halide perovskite solar cells. Devices containing perovskite thin films both with and without the potassium-halide (KI) treatment have been analyzed macroscopically for comparison. Through *J-V* measurements we show that the treated perovskite sample has a boost in the open-circuit

voltage (V_{oc}) and overall performance; yet, scanning electron microscopy (SEM) reveals surface aggregates on the treated sample. By resolving the nanoscale voltage response using KPFM we find that these surface precipitants have a unique work function behavior, and surprisingly, do not influence the local V_{oc}. From atomic force microscopy infrared (AFM-IR or nanoIR) measurements we identify and correlate the distinct work function response to the local chemical composition, revealing that a compound containing Br is embedded within the nanoscale surface aggregates. Finally, we implement 3D chemical imaging using ToF-SIMS to explore sub-surface chemical segregation and discover that the surface crystallites also contain high K concentrations, suggesting KBr as the chemical identity. Although the nanoIR and TOF-SIMS elemental detection ranges differ, we find traces of Br and K with each chemical imaging techniques, respectively, as KBr is transparent with IR light. With ToF-SIMS we find that the aggregates only conjugate at the top surface layer (first 10s of nm), and that the perovskite thin-film within the entire sample stack is otherwise chemically homogeneous. With these results we capture the infiltration pathways of the KI passivation, and while the overall passivation does increase PV performance macroscopically, this research reveals that additional optimization concerning the passivation process of both grain cores and boundaries could boost the solar cell power conversion efficiency further.

Results and Discussion

The perovskite samples under investigation are fabricated through a similar process as described in ref [6b], see also the Experimental Methods section for details. From the SEM images of both the Reference and KI-treated thin films, **Figure 1**a and b, respectively, we immediately discern a difference in surface morphology. While the Reference film is uniform and featureless, apart from the expected ~100 nm grains, the KI-treated sample shows bright, 1 – 2 μm diameter clusters, uniformly decorating the surface. These precipitants arise over time (from days to weeks), even when stored in inert conditions (see **Figure S1** of supporting

information), yet their influence on the local electrical properties is currently unclear. To explore the performance difference between the two samples, we fabricate full devices (see experimental section) and measure the macroscopic current density-voltage (*J-V*) curves for both the Reference and KI-treated devices under 1-sun illumination, provided in Figure 1c, see **Figure S2** in the supplemental information for the forward, reverse, and dark *J-V* curves for both devices. We note that the thin FTO/glass coverslip has a higher resistance than standard thick glass substrates and the Spiro-OMeTAD layer used here is approximately 4× thinner than in state-of-the-art devices, resulting in lower device performance. The thinner hole transport layer was used for all the microscopy measurements in order to have higher quality KFPM maps and to maintain good AFM tip quality, as the perovskite/probe interaction is prone to artefacts. The inset displays the layer-by-layer schematic of the solar cells. As expected, the passivated sample has a higher macroscopic V_{oc} and η due to the increased radiative recombination, detailed previously.[6b] The higher parasitic resistances that we measure in both of these *J-V* curves is caused by fabricating the devices on the cover-slip glass substrates (which are necessary for performing the following local electrical and chemical imaging measurements).

To investigate if the macroscopic V_{oc} can be further understood at that the nanoscale level, we implement KPFM. Briefly, original theorized by Lord Kelvin, KPFM measures the work function difference between the surface and the AFM probe (see **Figure S3**).[2a, 15] Upon illumination of a light-active material, the photovoltage is measured, and by subtracting a light KPFM map from a dark one, the quasi-Fermi level splitting remains, which is related to the V_{oc} to the semiconductor device.[3g] **Figure 2** presents KPFM under Dark and Light conditions on both the Reference (Figure 2a-d) and KI-treated (Figure 2e-h) half devices (without the top Au contact). To see the experimental setup of this and all follow experiments, see Figure S3 in the SI. The topography maps are consistent with the morphological features observed in the SEM images in Figure 1. Meanwhile, the local electrical measurements for each perovskite sample

display distinct voltage responses. Dark and illuminated KPFM maps on the Reference thin film (Figure 2b and c) reveal an expected homogeneous voltage response, as we are measuring along a high-mobility Sprio-OMeTAD surface, and this uniform voltage is typically ideal for solar cell materials.[3g] However, critically, the difference in photovoltage (ΔV, obtained from Light minus Dark scans), as shown by the voltage histograms plotted in Figure 2d, is only 330 mV (map provided in **Figure S4**d). In contrast, for the KI-treated sample the dark and light KPFM images (Figure 2f and g) show that the local contact potential difference (V_{CPD}) has more heterogeneity, indicating that the work function (and therefore, material) varies spatially. Specifically, regions with surface aggregates consistently have a lower V_{CPD} (≈500 mV) compared to the, again, isopotential perovskite thin-film stack. Despite this heterogeneity of the KI-treated sample, the overall photovoltage difference is 900 mV, much higher than the Reference sample (by 570 mV). This is in qualitative agreement with the macroscopic *J-V* curves in Figure 1c, where the KI-treated device has a larger V_{oc} than the Reference. To see the homogeneous surface photovoltage maps of both samples, (KFPM light minus dark), see supplemental materials Figure S4. Both the increased photovoltage and V_{oc} of the KI-treated film are evidence of successfully passivated films, however we note that the photovoltage value is different than the obtained macroscopic V_{oc} measured in Figure 1, which is due to an uncalibrated KPFM setup. In order to quantitatively compare these two amounts, we would need to account for the illumination area and intensity, charge extraction, and light absorption, detailed in refs [3e, 3g]; such calibration is beyond the scope of this work.

The nature of the low V_{CPD} regions in the KI-treated perovskite must originate from the passivation process[10] and are likely a different material, due to the evident 500 mV difference in V_{CPD}. To determine the nature of these features further, we implement nano-IR (or AFM-IR)[16], based on an AFM, which detects the chemical vibrational response with nanoscale spatial resolution[17]. During mapping, the intensity of a specified IR wavenumber is measured at each spatial coordinate (*x,y*) while simultaneously acquiring the surface topography. In

Figure 3a-h we display the resultant topography and IR absorption maps of the Reference and KI-treated samples. To determine the IR peak(s) of interest, prior to imaging, a broadband IR spectra is collected by sweeping the wavenumber of a quantum cascade laser chip, see Figure 3i. The lasers used in this experiment do not emit at all wavenumbers, therefore, there are regions where the counts are equal to zero on the graph, see Experimental Section for more details. We have selected wavenumbers = 1147 cm^{-1} and 1355 cm^{-1} for imaging (see supporting information **Figure S5, S6, and S7** for additional IR absorption maps), because while both the Reference and KI-treated samples contain a 1355 cm^{-1} peak, only the KI-treated perovskite exhibits the 1147 cm^{-1} IR absorption peak. The 1355 cm^{-1} peak designates the chemical compound cyclohexane (C_6H_{12}, likely linked to the Spiro-OMeTAD top layer) and the 1147 cm^{-1} peak is likely either: (i) Bromoform ($CHBr_3$) or (ii) bromopropyne (C_3H_3Br), based on the National Institute of Standards and Technology Chemistry WebBook Database.[18] From Figure 3a,e and c,g we find that the Reference perovskite has between 10-20 counts (equivalent to the noise level) in the 1147 cm^{-1} image, and the KI-treated film exhibits a strong, highly localized 1147 cm^{-1} vibration. Upon comparing the nano-IR map to its corresponding topography map, we find that the large 1147 cm^{-1} counts arise from the distinct surface aggregate sites. The 1355 cm^{-1} peak is detected in both the Reference and KI-treated films (Figure 3f and h). This vibrational mode has a uniform distribution in the Reference sample, while in the KI-treated sample, the Fouier-transform infrared spectroscopy (FTIR) signal is clearly anti-correlated to the surface aggregates. Note, the 1147 and 1355 cm^{-1} maps are purposely acquired in different (and representative) regions of the same sample, because both the IR laser and the AFM probe (which is in contact mode) can degrade the perovskite thin-film surface, see the supporting information Figure S7 for a study where we scanned the same region continuously. From Figure S7 we also demonstrate the excellent spatial resolution of this imaging technique, by resolving fine details of the surface aggregates. We also compare the nanoIR spectra to bulk FTIR measurements for both samples (see **Figure S8**), and find that many of the largest peaks in the

bulk FTIR spectra are also visible in the nanoscale spectra (e.g. 1000-1100 cm^{-1} and peaks in the 1300 cm^{-1} range). However, the 1147 cm^{-1} peak is not detected, likely due to its localization at the surface.

While nano-IR is extremely proficient at identifying chemical species at the nanoscale, it is a surface limited technique, reaching depths proportional to the diameter of the cantilever (here, 20 – 50 nm). To further understand the full effect of the KI passivation treatment, we now turn to time-of-flight secondary ion mass spectroscopy (ToF-SIMS), based in a scanning electron microscope (SEM).[19] Here, a Ga^+ ion beam bombards the perovskite films, systematically etching away the top few nanometers of the material with each pass. This approach enables chemical identification in 3D with an *x,y* spatial resolution of ~100 nm, therefore, compositional variations on the grain-to-grain length scale cannot be resolved. In **Figure 4** we show depth profiles obtained from TOF-SIMS (for additional depth profiles of each sample, see supporting information, **Figure S9**). As expected, the Reference sample, Figure 4a, has no K within the entire layer stack. However, for the KI-treated perovskite there is initially a small K peak at the top surface of the film, Figure 4b, which then decays at the start of the Spiro layer, and ultimately maximizes in the perovskite absorbing layer (~150 – 250 seconds). This is evidence that some excess K has migrated to the top surface of the film, while entirely bypassing the Spiro layer between the perovskite material and the surface. Note, the layer assignments above the depth profiles in Figure 4 are approximate, and based on the onset of the elements that are expected to be present within the layer. Besides the presences of the K element, the depth profiles of both thin films are very similar. The Br-1/Br-2 and Spiro-1/Spiro-2 curves refer to different isotopes of the Br/Spiro compounds.

We acquired TOF-SIMS *x,y* images of the local elemental distribution with a spatial resolution of ~100 nm. The 3D TOF-SIMS data displaying the local K concentration for the KI-treated perovskite are presented in **Figure 5** (for multiple 3D TOF-SIMS maps and the distribution of iodine for both the Reference and KI-treated sample, see **Figure S10 and S11**

in the supporting information). Figure 5a and b display the top-most layer of this perovskite thin-film stack, where a heterogeneous K distribution is revealed. The dimensions of the K features on the top surface of the entire sample stack, (yellow patches in Figure 5a), in the TOF-SIMS data are nearly identical to those identified with SEM, AFM, and nano-IR, indicating strong evidence of the passivation treatment inducing chemical migration. The diffusion of K to the surface signifies that there is excess K ions which gets pushed out of the perovskite layer, which may be why performance degrades with larger K inclusion, as shown in ref 17. Surprisingly, there is negligible K found in the Spiro-OMeTAD layer, while the chemical distribution within the perovskite itself is uniform (Figure 5d and e), yet there is some slight K variation at both the HTM/perovskite and perovskite/ETM interfaces (panel 5c and 5f, respectively). All other elemental distributions of the thin film layer stack are homogeneous throughout the perovskite film, at least within the spatial resolution of our measurements. Interestingly, there is no signature of Br at the surface of the KI-treated perovskite (see **supporting video S1**) in TOF-SIMS, as it has been suggested on our nanoIR measurements presented in Figure 3. While, on the nanoIR setup, there is no peak assignable to K or K-containing compounds in the FTIR spectra. This may be due to the difference in sensitivity between two detection setups, as well as the detection windows. For example, if the aggregates contain the compound KBr, this would not show up in the nanoIR data, as KBr is a common material used as infrared transmission windows.[20]

The microscopy experiments presented here deliver an insightful characterization platform, producing a complete narrative for the inter-relations between the electrical and chemical properties of optoelectronic materials at the nanoscale. These measurements are adaptable for a variety of optoelectronic systems beyond perovskites, such as other complex tandem solar cells,[21] and organic light-emitting diodes.[22] Such datasets on halide perovskite materials, coupled with other local material property experiments such as EDX,[10] nano X-ray diffraction[23] or electron diffraction imaging,[24] would extend correlative microscopy, linking

structural-chemical-electrical properties, a 'holy-grail' approach that would unlock a deep understanding of the performance heterogeneities that currently limit the η in halide perovskites.[2b]

Conclusion

We provided experimental evidence for how a state-of-the-art KI defect passivation treatment, known to macroscopically boost V_{oc} of perovskite solar cells, infiltrates and is distributed within a perovskite layer by implementing high spatial resolution mapping techniques. All data are compared with a Reference sample that has not been subjected to the passivation processing step. With KPFM we showed how the local voltage measurements display a heterogeneous work function for the KI-treated sample, with variations in work function up to 500 mV. However, despite this variation, the surface photovoltage distribution was homogenous, evidenced by performing illuminated-KPFM, indicating the precipitants do not locally harm or boost performance. Surface chemical properties at the nanoscale, realized with nano-IR experiments, revealed that the surface aggregates on the KI-treated sample were assigned to wavenumber 1147 cm^{-1}, which is linked to a Br-containing chemical. For 3D elemental mapping, we applied ToF-SIMS and found that while there is heterogeneity in the K concentration at the sample surface, the distribution of K within the perovskite layer is uniform. These findings are an indicator that excess KBr has migrated out of the perovskite layer naturally over time towards the surface of the sample stack. By using multi-property studies on this by-product, we determine that a slightly smaller concentration of the KI additive treatment might boost the device performance. This alteration of the processing would enable a uniform surface work function, while also maintaining the benefits of a higher V_{oc} photovoltaic device due to passivated interfaces (e.g. grain boundaries) within the perovskite layer.

Experimental Section

Thin film and solar cell fabrication: All the organic cation salts were purchased from Dyesol, the lead compounds for TCI Chemicals, and CsI and KI from Alfa Aesar. Spiro-OMeTAD was purchased from Borun Chemicals and used as received. Unless otherwise stated, all other materials were purchased from Sigma-Aldrich.

The triple cation–based perovskite [i.e. $Cs_{0.06}FA_{0.79}MA_{0.15}Pb(I_{0.85}Br_{0.15})_3$] was prepared by dissolving PbI_2 (1.2 M), FAI (1.11 M), MABr (0.21 M), and $PbBr_2$ (0.21 M) in a mixture of anhydrous N, N′-dimethylformamide/dimethyl sulfoxide (DMF/DMSO) (4:1, volume ratios), followed by the addition of 5% (v/v) CsI stock solute (1.5 M in DMSO). To fabricate the potassium passivated triple cation perovskite, we added 10% (v/v) from KI stock solution (1.5M in DMF/DMSO; 4:1, volume ratios) to the triple cation perovskite solution. We then spin-coated the perovskite solutions using a two-step program at 2000 and 4000 rpm for 10 and 35 s, respectively, and dripping 110 μl of chlorobenzene after 30 s. We then annealed the films at 100°C for one hour. All the film preparations were performed in a nitrogen-filled glove box and the same procedures for substrate preparation and deposition of both the TiO_2 and Spiro-OMeTAD layers is detailed in our previous work.[6b] For the full devices, thermally evaporated 80 nm of Au at an evaporation rate of 0.05 nm s^{-1} was deposited onto the surface.

Current-voltage photovoltaic characterization: Current-voltage characteristics were recorded at the University of Cambridge, prior to being sent to the University of Maryland for microscopic characterization (to avoid air exposure, samples were couriered and stored in nitrogen and Ar atmospheres, respectively). An external potential bias was applied to the cell while recording the generated photocurrent with a digital source meter (model 2400, Keithley Instruments). The light source was a 450-W xenon lamp (Oriel) equipped with a Schott K113 Tempax sunlight filter (Praezisions Glas & Optik GmbH) to match the emission spectrum of the lamp to the AM1.5G standard. Before each measurement, the exact light intensity was determined using a calibrated Si reference diode equipped with an infrared cutoff filter (KG-3, Schott). All measurements were conducted using a non-reflective metal aperture of 0.105 cm^2

to define the active area of the device and avoid light scattering through the sides. The incident light intensity was adjusted to 1000 W m^{-2} in accordance with standard AM 1.5 reporting conditions. The voltage scan rate was 10 mV s^{-1} and no device preconditioning, such as light soaking or extended forward voltage biasing in the dark, was applied before starting the measurement.

Scanning electron microscopy images: We used a Tescan GAIA3 FIB/SEM instrument to acquire the images displayed in Figure 1. The acceleration voltage = 5 kV, at a magnification of ≈10 kx was used to acquire images in SE mode of both the Reference and KI-treated samples with a working distance of 5.15 and 5.68 mm, respectively.

Kelvin probe force microscopy: The perovskite samples were measured using an Asylum Cypher, where the bottom FTO contact was grounded with respect to the Pt-coated AFM probe. The tip scanned the surface of the 50-nm thick Spiro-OMeTAD hole-transport material. We implemented heterodyne KPFM imaging mode[3e, 25] and during the illuminated KPFM measurements a 532 nm laser with a 1-sun photon flux density illuminated through the glass/FTO side of the sample. That is, on the opposite side of the scanning AFM tip, thus, avoiding shadowing effects from the probe. Note: the power stability of the laser used in these measurements = ±0.5%. A flow a dry-air was coupled into the AFM chamber to keep the humidity level <10% during the measurements.

Nano-IR measurements: Nanoscale chemical measurements were performed at the Center of Nanophase Materials Science at Oak Ridge National Lab in Oak Ridge, TN, USA. We acquired the local nano-IR spectra and chemical maps with the NanoIR2-s Anasys Instruments microscope in contact mode. An initial 'array' of nano-IR spectra is taken for each sample to determine the presence of specific IR absorption peaks and whether these peaks varied as a function of location on the sample surface. Subsequently, IR absorption peaks that were found to be relatively strong or varied as a function of location across the sample surface in the array were chemically mapped. Any vibration changes are detected by the scanning probe tip, which

is scanning the 50-nm Spiro-OMeTAD surface of the entire perovskite sample stack. The IR laser incident on the sample surface has a spot size, on average, of 62 μm. The instrument is equipped with a quantum cascade laser that is tunable for the wavenumbers ranges: 920-1174 cm^{-1}, 1310-1411 cm^{-1}, and 1505-1863 cm^{-1}. All measurements were performed in ambient conditions. Nano-IR AFM probes (Anasys Instruments) are Au coated with a nominal spring constant of 3 N/m and radius of curvature of > 25 nm. The probe diameter, which is proportional to the probe depth of the nano-IR measurement, was between 20-50 nm. Figure 3, S5 and S6 were acquired for 15 min/map, and Figure S7 for 9 min/map.

ToF-SIMS characterization: Using the same Tescan GAIA3 SEM/FIB setup as describe above, we bombarded the perovskite samples with a focused Ga^+ ion beam at 20 keV and with a current of 1nA, which served as both the primary and sputtering beam. Both the positive and negative secondary ions were generated by ionizing the sample with the Ga^+ beam. The ToF-SIMS signals were detected by a mass spectrometer. During the measurements, the vacuum level was kept below 10^{-4} Torr at all times. Three different locations on each perovskite sample were measured for statistical purposes. Areas of 20 × 20 μm^2 were sputtered away for secondary ion determination, while 15 × 15 μm^2 central regions were analyzed to avoid any edge effect. The lateral spatial resolution is 100 nm, while the depth resolution is <10 nm.

Supporting Information

Supporting Information is available from the Wiley Online Library or from the author.

Acknowledgements

The nano-IR portion of this research was conducted at the Center for Nanophase Materials Sciences, which is a DOE Office of Science User Facility. We acknowledge the support of the Maryland NanoCenter, its FabLab, and its AIMLab. M.S.L. acknowledges the financial support from ECCS-NSF (award 16-10833). E.M.T. thanks UMD All-S.T.A.R. Fellowship 2017-2018,

and the Hulka Energy Research Fellowship 2017-2018 for funding support. M.A.-J. thanks Cambridge Materials Limited and EPSRC (Grant Number: EP/M005143/1) for their funding and technical support. S.D.S. and K.J. thank the Royal Society for funding. J.L.G. and J.N.M. thank the National Science Foundation CAREER Grant No. ECCS-1554503 and the Office of Naval Research YIP Award Grant No. N00014-16-1-2540.

ORCIDs:

E. M. Tennyson: 0000-0003-0071-8445
M. Abdi-Jalebi: 0000-0002-9430-6371
K. Ji: 0000-0002-1278-3212
J. Garrett: 0000-0001-8265-0661
C. Gong: 0000-0003-3302-7675
A. A. Pawlicki: 0000-0001-6843-3353
O. S. Ovchinnikova: 0000-0001-8935-2309
J. N. Munday: 0000-0002-0881-9876
S. D. Stranks: 0000-0002-8303-7292
M. S. Leite: 0000-0003-4888-8195

Notes: The authors declare no competing financial interest.

Received: ((will be filled in by the editorial staff))
Revised: ((will be filled in by the editorial staff))
Published online: ((will be filled in by the editorial staff))

References

[1] D. B. Mitzi, *Chem. Rev.* **2019**, *5*, 3033.

[2] a) E. M. Tennyson, C. Gong and M. S. Leite, *ACS Energy Lett.* **2017**, *12*, 2761; b) E. M. Tennyson, T. A. S. Dohertry and S. D. Stranks, *Nat. Rev. Mater.* **2019**, 573; c) S. I. Seok, M. Grätzel and N.-G. Park, *Small* **2018**, *20*, 1704177; d) J. Hieulle, C. Stecker, R. Ohmann, L. K. Ono and Y. Qi, *Small Methods* **2018**, *1*, 1700295; e) J. M. Howard, R. Lahoti and M. S. Leite, *Adv. Energy Mater.* **2019**, 1903161.

[3] a) J. M. Howard, E. M. Tennyson, B. R. Neves and M. S. Leite, *Joule* **2018**, *2*, 325; b) T. Leijtens, K. Bush, R. Cheacharoen, R. Beal, A. Bowring and M. D. McGehee, *J. Mater.*

Chem. A **2017**, *23*, 11483; c) N.-G. Park, M. Grätzel, T. Miyasaka, K. Zhu and K. Emery, *Nat. Energy* **2016**, 16152; d) E. M. Tennyson, B. Roose, J. L. Garrett, C. Gong, J. N. Munday, A. Abate and M. S. Leite, *ACS Nano* **2018**, *2*, 1538; e) J. L. Garrett, E. M. Tennyson, M. Hu, J. Huang, J. N. Munday and M. S. Leite, *Nano Lett.* **2017**, *4*, 2554; f) E. M. Tennyson, J. M. Howard and M. S. Leite, *ACS Energy Lett.* **2017**, 1825; g) E. M. Tennyson, J. L. Garrett, J. A. Frantz, J. D. Myers, R. Y. Bekele, J. S. Sanghera, J. N. Munday and M. S. Leite, *Adv. Energy Mater.* **2015**, *23*, 1501142.

[4] a) L. Li, N. Liu, Z. Xu, Q. Chen, X. Wang and H. Zhou, *ACS Nano* **2017**, *9*, 8804; b) B. Roose, Q. Wang and A. Abate, *Adv. Energy Mater.* **2018**, *5*, 1803140.

[5] L. K. Ono, Y. Qi and S. Liu, *Joule* **2018**, *10*, 1961.

[6] a) F. Wang, S. Bai, W. Tress, A. Hagfeldt and F. Gao, *npj Flexible Electron.* **2018**, *1*, 22; b) M. Abdi-Jalebi, Z. Andaji-Garmaroudi, S. Cacovich, C. Stavrakas, B. Philippe, J. M. Richter, M. Alsari, E. P. Booker, E. M. Hutter, A. J. Pearson, S. Lilliu, T. J. Savenije, H. Rensmo, G. Divitini, C. Ducati, R. H. Friend and S. D. Stranks, *Nature* **2018**, 497; c) M. T. Klug, A. Osherov, A. A. Haghighirad, S. D. Stranks, P. R. Brown, S. Bai, J. T. W. Wang, X. Dang, V. Bulović, H. J. Snaith and A. M. Belcher, *Energy Environ. Sci.* **2017**, *1*, 236; d) B. Li, Y. Zhang, L. Fu, T. Yu, S. Zhou, L. Zhang and L. Yin, *Nat. Commun.* **2018**, *1*, 1076.

[7] a) B.-w. Park, N. Kedem, M. Kulbak, D. Y. Lee, W. S. Yang, N. J. Jeon, J. Seo, G. Kim, K. J. Kim, T. J. Shin, G. Hodes, D. Cahen and S. I. Seok, *Nat. Commun.* **2018**, *1*, 3301; b) D. H. Cao, C. C. Stoumpos, C. D. Malliakas, M. J. Katz, O. K. Farha, J. T. Hupp and M. G. Kanatzidis, *APL Mater.* **2014**, *9*, 091101.

[8] X. Zheng, B. Chen, J. Dai, Y. Fang, Y. Bai, Y. Lin, H. Wei, Xiao C. Zeng and J. Huang, *Nat. Energy* **2017**, 17102.

[9] F. Zheng, W. Chen, T. Bu, K. P. Ghiggino, F. Huang, Y. Cheng, P. Tapping, T. W. Kee, B. Jia and X. Wen, *Adv. Energy Mater.* **2019**, *24*, 1901016.

[10] M. Abdi-Jalebi, Z. Andaji-Garmaroudi, A. J. Pearson, G. Divitini, S. Cacovich, B. Philippe, H. Rensmo, C. Ducati, R. H. Friend and S. D. Stranks, *ACS Energy Lett.* **2018**, *11*, 2671.

[11] a) S. Ye, H. Rao, Z. Zhao, L. Zhang, H. Bao, W. Sun, Y. Li, F. Gu, J. Wang, Z. Liu, Z. Bian and C. Huang, *J. Am. Chem. Soc.* **2017**, *22*, 7504; b) A. Abate, M. Saliba, D. J. Hollman, S. D. Stranks, K. Wojciechowski, R. Avolio, G. Grancini, A. Petrozza and H. J. Snaith, *Nano Lett.* **2014**, *6*, 3247; c) R. Wang, J. Xue, L. Meng, J.-W. Lee, Z. Zhao, P. Sun, L. Cai, T. Huang, Z. Wang, Z.-K. Wang, Y. Duan, J. L. Yang, S. Tan, Y. Yuan, Y. Huang and Y. Yang, *Joule* **2019**, *6*, 1464.

[12] Y. Almadori, D. Moerman, J. L. Martinez, P. Leclère and B. Grévin, *Beilstein J. Nanotechnol.* **2018**, 1695.

[13] L. Wang, H. Wang, M. Wagner, Y. Yan, D. S. Jakob and X. G. Xu, *Sci. Adv.* **2017**, *6*, 1.

[14] J. Kong, R. Giridharagopal, J. S. Harrison and D. S. Ginger, *J. Phys. Chem. Lett.* **2018**, *12*, 3307.

[15] a) L. Kelvin, *Philosophical Magazine* **1898**, *82*, 66; b) M. Nonnenmacher, M. P. O'Boyle and H. K. Wickramasinghe, *Appl. Phys. Lett.* **1991**, *25*, 2921.

[16] A. Dazzi and C. B. Prater, *Chem. Rev.* **2017**, *7*, 5146.

[17] R. Szostak, J. Silva, S.-H. Turren-Cruz, M. Soares, R. Freitas, A. Hagfeldt, H. Tolentino and A. Nogueira, *Sci. Adv.* **2019**, *10*, eaaw6619.

[18] *NIST Chemistry WebBook, NIST Standard Reference Database Number 69*, National Institute of Standards and Technology, Gaithersburg MD, 20899 **2019**.

[19] S. P. Harvey, Z. Li, J. A. Christians, K. Zhu, J. M. Luther and J. J. Berry, *ACS Appl. Mater. Inter.* **2018**, *34*, 28541.

[20] T. F. Deutsch, *J. Phys. Chem. Solids* **1973**, *12*, 2091.

[21] a) D. H. Kim, C. P. Muzzillo, J. Tong, A. F. Palmstrom, B. W. Larson, C. Choi, S. P. Harvey, S. Glynn, J. B. Whitaker, F. Zhang, Z. Li, H. Lu, M. F. A. M. van Hest, J. J. Berry, L. M. Mansfield, Y. Huang, Y. Yan and K. Zhu, *Joule* **2019**, *7*, 1734; b) F. Sahli, J. Werner, B. A. Kamino, M. Bräuninger, R. Monnard, B. Paviet-Salomon, L. Barraud, L. Ding, J. J. Diaz Leon, D. Sacchetto, G. Cattaneo, M. Despeisse, M. Boccard, S. Nicolay, Q. Jeangros, B. Niesen and C. Ballif, *Nat. Mater.* **2018**, *9*, 820.

[22] J. Song, T. Fang, J. Li, L. Xu, F. Zhang, B. Han, Q. Shan and H. Zeng, *Adv. Mater.* **2018**, *50*, 1805409.

[23] J.-P. Correa-Baena, Y. Luo, T. M. Brenner, J. Snaider, S. Sun, X. Li, M. A. Jensen, N. T. P. Hartono, L. Nienhaus, S. Wieghold, J. R. Poindexter, S. Wang, Y. S. Meng, T. Wang, B. Lai, M. V. Holt, Z. Cai, M. G. Bawendi, L. Huang, T. Buonassisi and D. P. Fenning, *Science* **2019**, *6427*, 627.

[24] M. U. Rothmann, W. Li, J. Etheridge and Y.-B. Cheng, *Adv. Energy Mater.* **2017**, *23*, 1700912.

[25] J. L. Garrett and J. N. Munday, *Nanotechnology* **2016**, *24*, 245705.

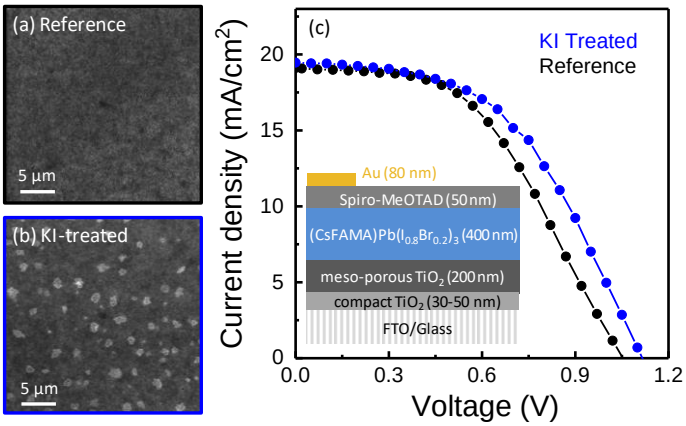

Figure 1. Macroscopic characterization of perovskite thin films and devices. SEM image of (a) the Reference, triple cation/mixed halide and (b) the KI-treated thin films with the same perovskite (CsFAMA)Pb($I_{0.85}Br_{0.15}$)$_3$ composition. (c) Reverse bias macroscopic light *J-V* curves of the Reference (black) and KI-treated (blue) perovskite solar cells. Inset: layer-by-layer schematic of perovskite devices; out of scale for clarity. Figures-of-merit for the reference sample: V_{oc} = 1.05 V, J_{sc} = 18.43 mA/cm^2, *FF* = 48%, and η = 9.3% (in reverse bias); KI-treated sample: V_{oc} = 1.13 V, J_{sc} = 19.46 mA/cm^2, *FF* = 50%, and η =11.0% (in reverse bias).

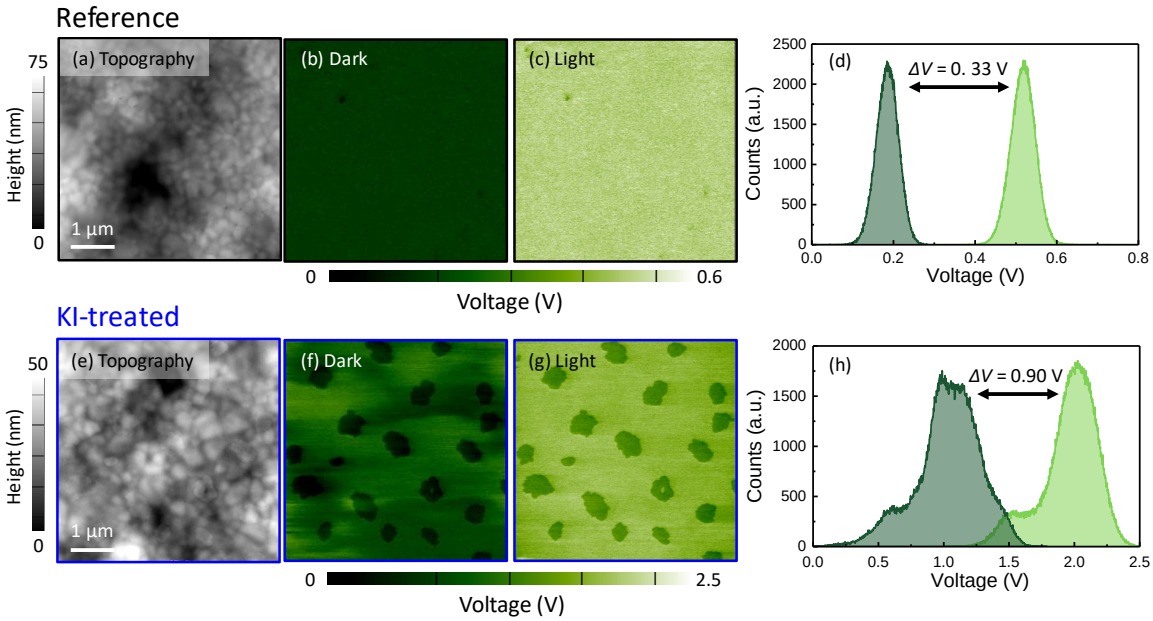

Figure 2. Local voltage response in perovskites. For the Reference perovskite device: (a) 5 × 5 µm^2 topography and (b,c) Kelvin probe force microscopy (KPFM) images in both dark and illuminated conditions, respectively. (d) Voltage histograms for the KPFM maps in (b,c). For the KI-treated sample: (e) Topography and (f,g) dark and light KPFM images, respectively, and (h) the associated voltage histograms for both KPFM maps. Illumination conditions: 532 nm laser under 1-sun illumination, spot size = 500 µm in diameter. The ΔV in the histograms

denotes the average value of the difference between the light and dark KPFM maps. The magnitude of ΔV is related to the macroscopic open-circuit voltage (V_{oc}) of the perovskite.

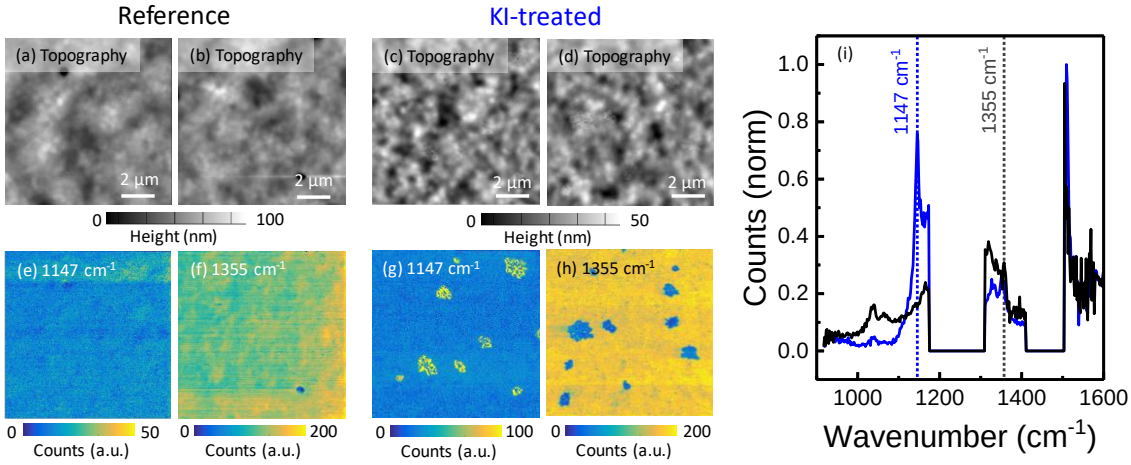

Figure 3. Resolving the chemical composition distribution of KI-passivated perovskites. (a-d) Topography map and (e-h) simultaneously acquired nano-IR measurements on Reference and KI-treated perovskite samples. In (e,g) it is evident that the wavenumber 1147 cm^{-1} has a negligible presence in the Reference samples, meanwhile, it is directly related to the surface aggregates (faintly observed in the above topography map). Wavenumber 1355 cm^{-1} has a higher abundance in both samples and is anti-correlated to the surface aggregates in the KI-treated perovskite film. (i) Nano-FTIR spectra acquired on the Reference (black) and KI-treated (blue) samples. The blue spectrum shown in (i) was acquired while the probe was hovering above a surface aggregate for the KI-sample.

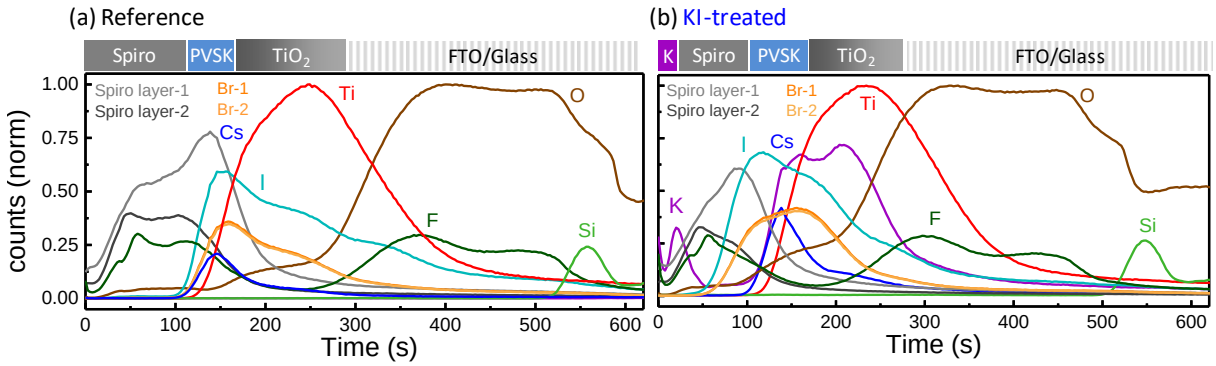

Figure 4. Time-of-flight secondary ion mass spectroscopy (TOF-SIMS) depth profiles. The average elemental distribution for the (a) Reference and (b) KI-treated perovskite thin films as a function of depth within a 15 × 15 × 1 μm^3 excavated volume. Note that each sample's depth profiles are individually normalized relative to the ion (+ or -) with the highest number of counts. For example, because Ti^+ has the highest detected counts, and all other + ions are

normalized with respect to Ti^+. Further, the counts for K on the Reference samples are within the noise level of the TOF-SIMS measurement.

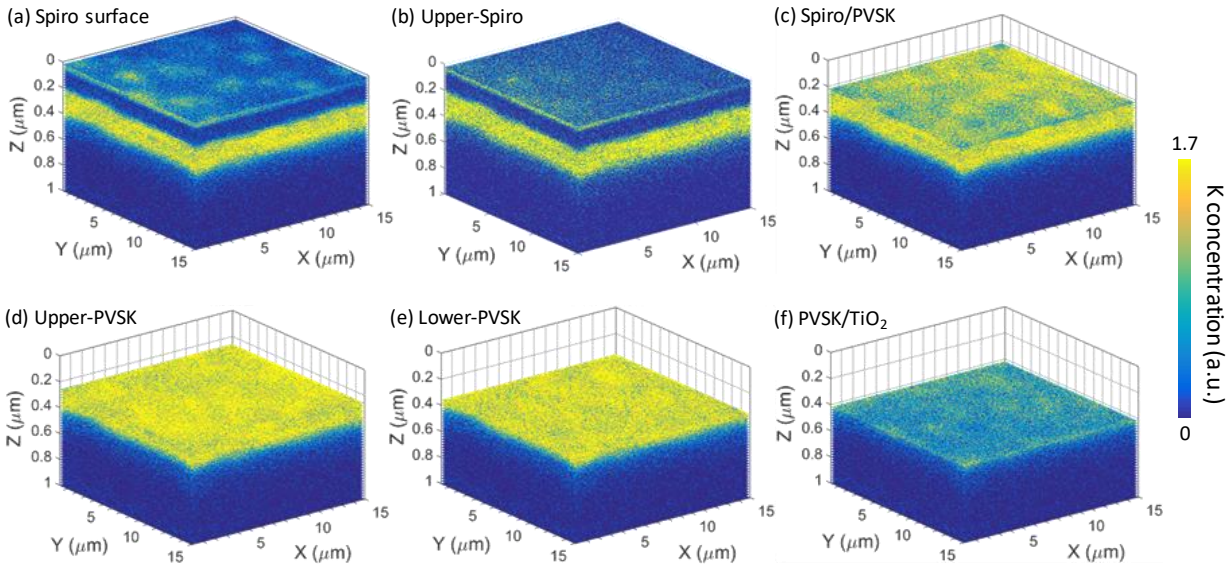

Figure 5. Distribution of K as a function of depth within the KI-treated perovskite sample. (a) TOF-SIMS map of entire sample stack. Note the heterogeneous distribution of K (yellow patches) at the top surface of thin-film, which are directly related to the surface aggregates measured by KPFM and nano-IR measurements. (b) TOF-SIMS map acquired a few nanometers below the top surface, where the K concentration wanes. (c) TOF-SIMS map at the top surface of the perovskite layer, where a semi-uniform K distribution followed by (d,e) higher uniformity deeper into the perovskite layer (here, d and e, represent the upper and lower part of the perovskite layer, respectively). (f) TOF-SIMS map showing K concentration at the interface between the perovskite and TiO_2 layers, with slight heterogeneities. Note: the *z*-axis displayed here is approximate, as the sputtering speed is highly material dependent.

Table of contents entry:

A correlative study that investigates the influence of the novel KI-passivation treatment on halide perovskite solar cell materials. By comparing the local electrical and chemical properties using an array of high-spatial resolution imaging techniques, this research shows the migration of excess passivation solution and links the nanoscale properties with macroscopic device performance.

Keyword correlative microscopy

Correlated Electrical and Chemical Nanoscale Properties in Potassium-Passivated, Triple-Cation Perovskite Solar Cells

*Elizabeth M. Tennyson, Mojtaba Abdi-Jalebi, Kangyu Ji, Joseph L. Garrett, Chen Gong, Alison A. Pawlicki, Olga S. Ovchinnikova, Jeremy N. Munday, Samuel D. Stranks, Marina S. Leite**

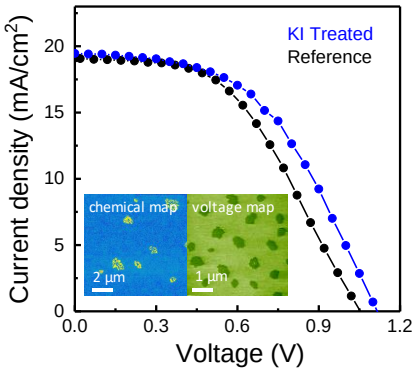

Supporting Information

Correlated Electrical and Chemical Nanoscale Properties in Potassium-Passivated, Triple-Cation Perovskite Solar Cells

*Elizabeth M. Tennyson, Mojtaba Abdi-Jalebi, Kangyu Ji, Joseph L. Garrett, Chen Gong, Alison A. Pawlicki, Olga S. Ovchinnikova, Jeremy N. Munday, Samuel D. Stranks, Marina S. Leite**

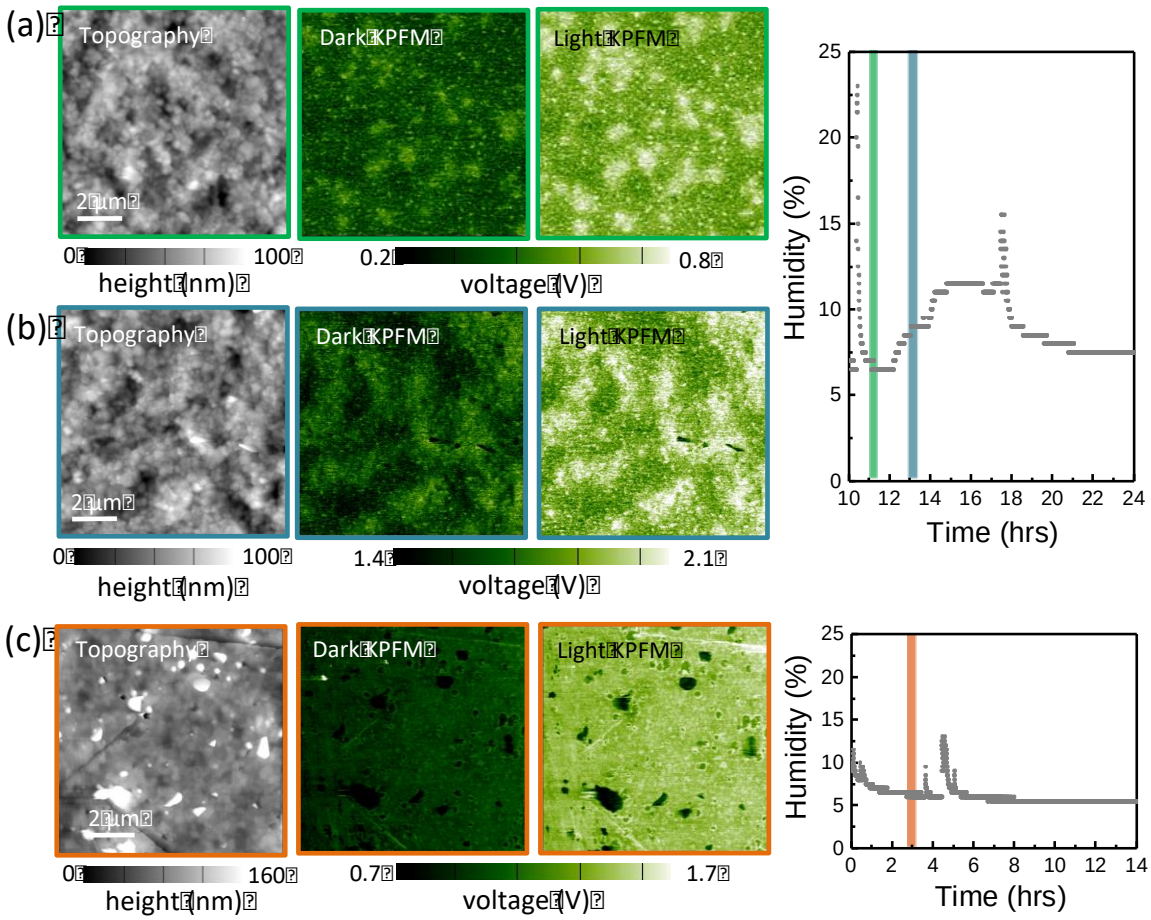

Figure S1. (a) Topography, dark- and light-Kelvin probe force microscopy (KPFM) measurements on a fresh KI-treated sample which was (b) gradually exposed to moisture in humidity-controlled AFM chamber. The green and blue lines on the real-time humidity data indicate when the KPFM measurements of (a) and (b) were performed, respectively. Surface features begin to precipitate with humidity exposure. (c) Topography, dark- and light-KPFM measurements on an identical KI-treated sample which was stored in Ar atmosphere glove box for one week and subsequently measured (bottom row). Surface aggregates also develop with time, without any external inducers (e.g. moisture, temperature or light). Orange region on the

real-time humidity data for this sample indicates when the KPFM measurements shown here were acquired. Illumination light source used: 532 nm with a 1-sun equivalent photon flux.

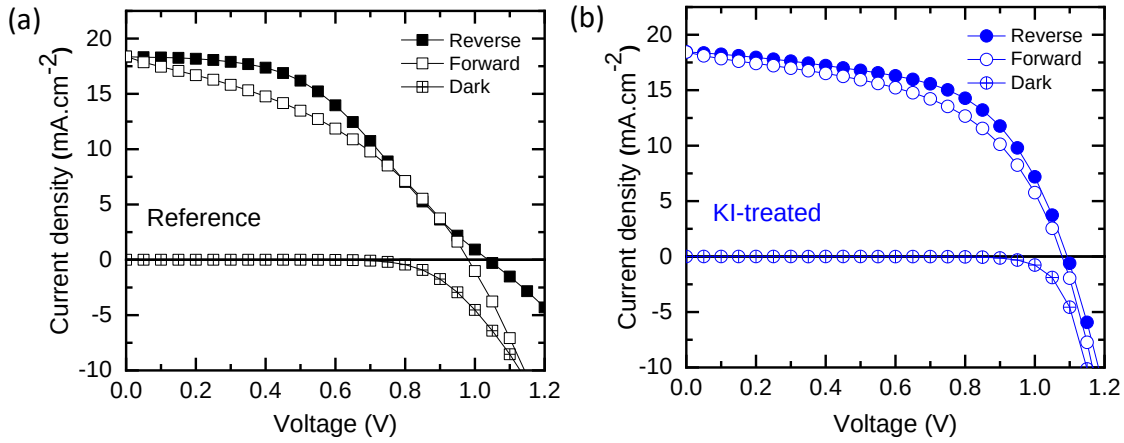

Figure S2. Light (AM1.5G 1-sun illumination) and Dark *J-V* curves for (a) Reference and (b) KI-treated solar cell devices. For the entire solar cell stack, see Figure 1 of the main manuscript. For the reference sample: V_{oc} = 1.04 V, J_{sc} = 18.35 mA/cm^2, *FF* = 44 %, and η = 8.4 % (in reverse bias); KI-treated sample: V_{oc} = 1.09 V, J_{sc} = 18.46 mA/cm^2, *FF* = 57 %, and η =11.4 % (in reverse bias).

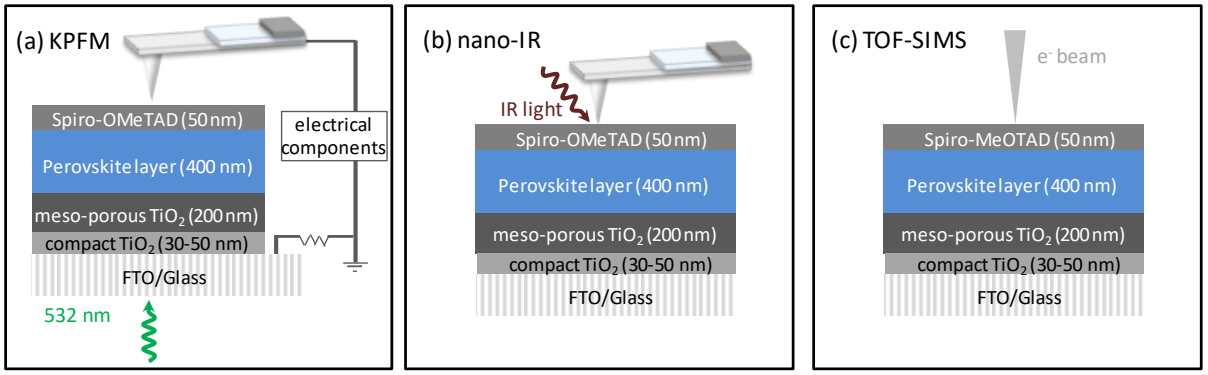

Figure S3. Cross-sectional schematic of the three different microscopy techniques implemented within this manuscript (a) KPFM, (b) nano-IR, and (c) TOF-SIMS.

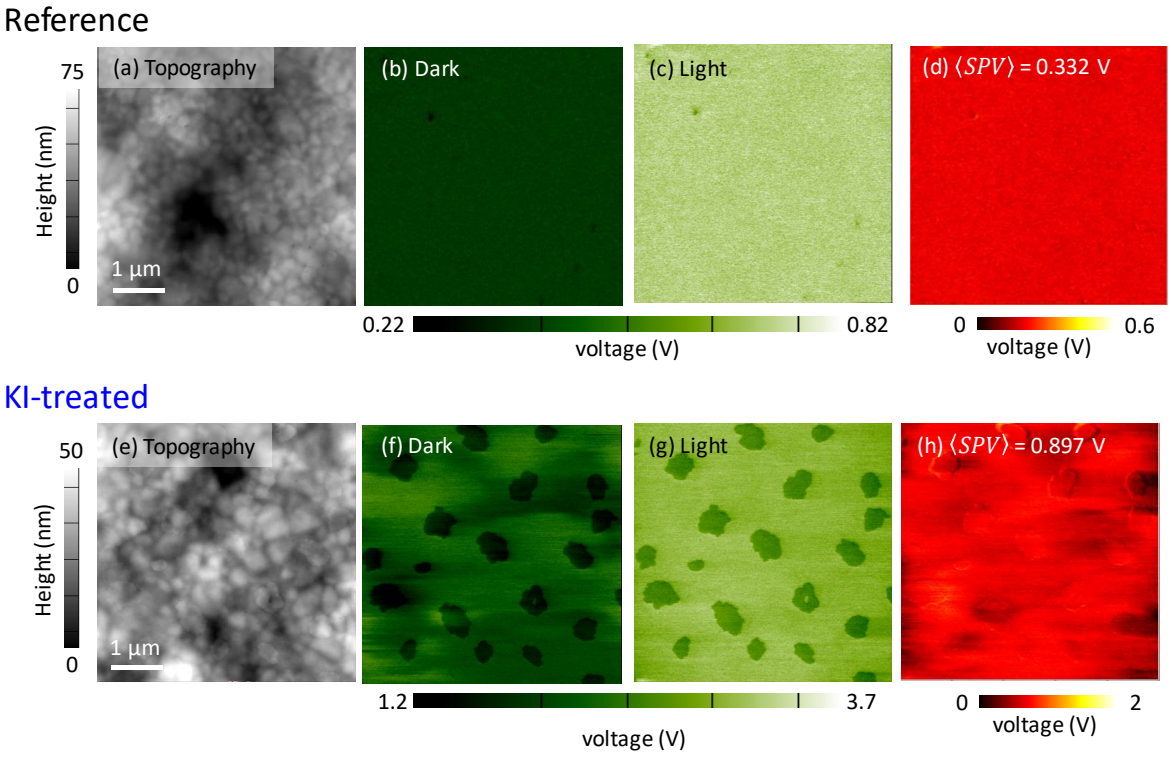

Figure S4. KPFM measurements on the (a-d) Reference and (e-h) KI-treated perovskite half devices. (a) Topography and simultaneous (b) Dark and (c) Light KPFM measurements of the Reference sample. (d) The surface photovoltage (SPV) of the KPFM measurements, which is the Light KPFM map subtracted by the Dark KPFM map. (e) Topography and (f) Dark and (g) Light KPFM maps of the KI-treated sample. In (h) the SPV map is displayed. The average SPV value for the entire map is indicated for both samples.

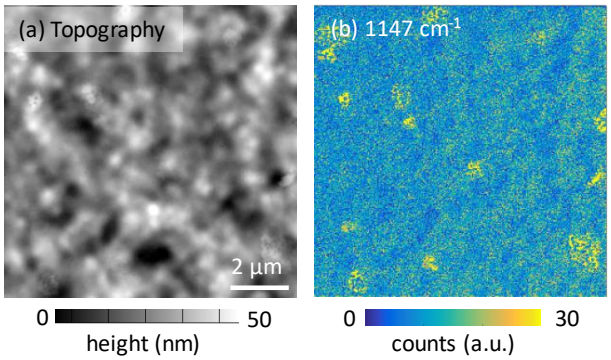

Figure S5. (a) Topography and simultaneous (b) nano-IR at 1147 cm^{-1} acquired on another location of the KI-treated sample.

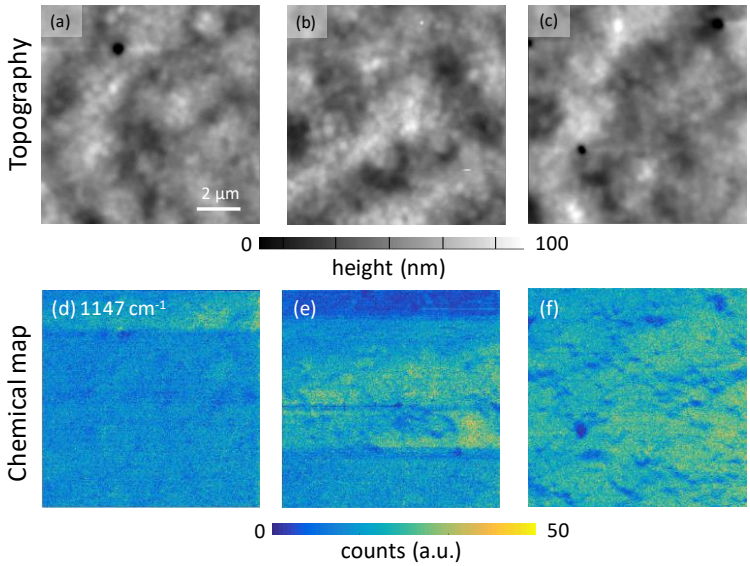

Figure S6. (a-c) Topography and simultaneous (d-f) nano-IR at 1147 cm^{-1} acquired on multiple regions of a Reference sample.

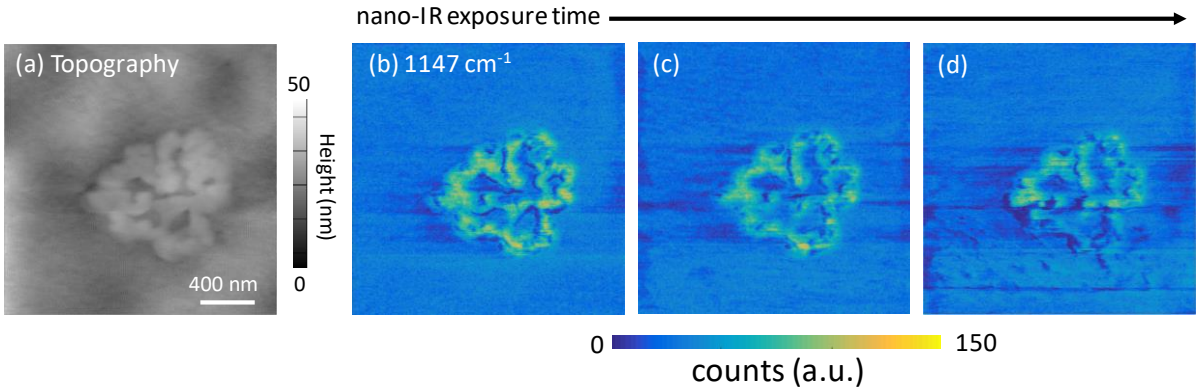

Figure S7. (a) Initial topography scan and simultaneously acquired (b) nano-IR map. (c) and (d) are the subsequent nano-IR images, demonstrating how with continuous IR exposure degrades the sample surface, the duration of each nanoIR measurement is ≈9 min for a total exposure time of 27 min.

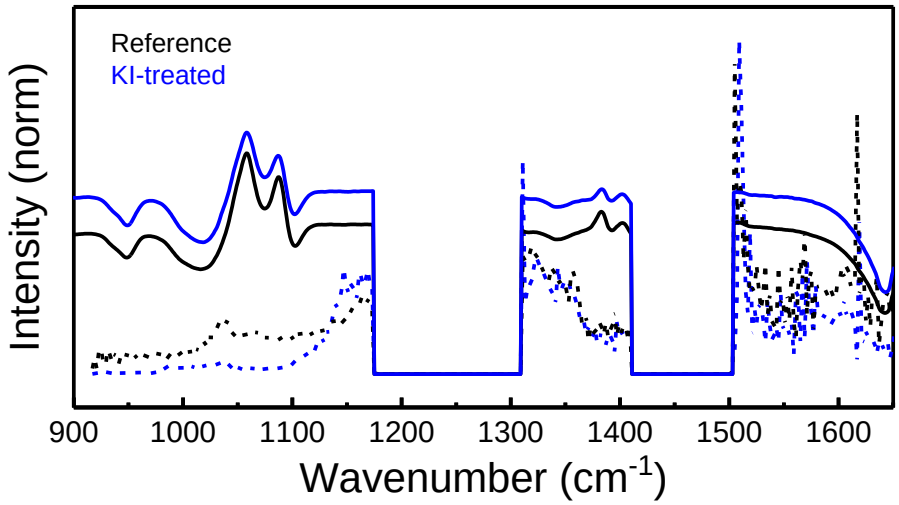

Figure S8. Normalized bulk FTIR vs nanoIR (dashed) spectra. Macroscopic FTIR measurements were performed on perovskite films that were drop casted on a KBr transparent KBr window. Data from 1175 – 1309 cm^{-1} and 1411 – 1503 cm^{-1} was removed to easily compare between the two different techniques. The surface aggregate feature at 1147 cm^{-1} is not present in the bulk FTIR spectrum due to the lack of surface sensitivity in the bulk FTIR measurement.

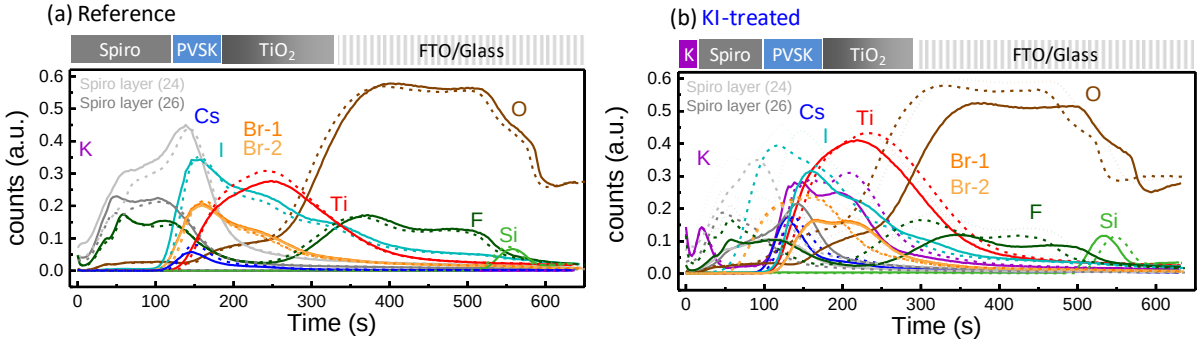

Figure S9. Time of flight-secondary ion mass spectroscopy depth profiles in multiple locations for the (a) Reference and (b) KI-treated thin film samples. No normalization was performed.

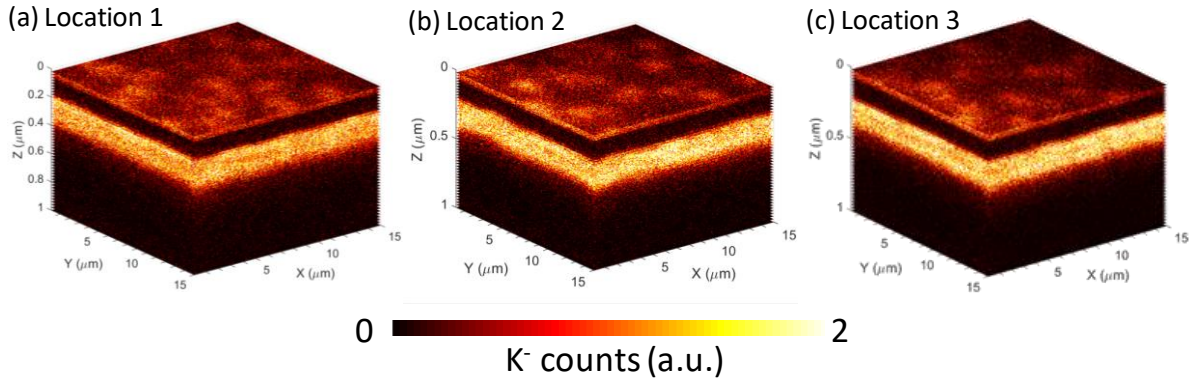

Figure S10. (a-c) Time of flight-secondary ion mass spectroscopy 3D maps of the distribution of the K element in multiple locations for the KI-treated perovskite sample.

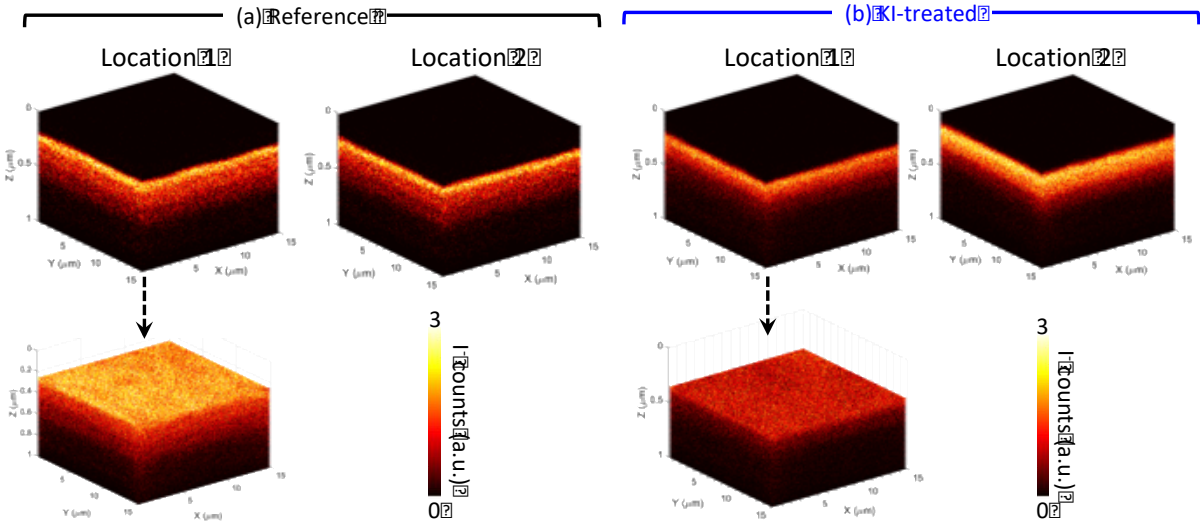

Figure S11. Time of flight-secondary ion mass spectroscopy 3D maps of the distribution of iodine in multiple locations for the (a) Reference and (b) KI-treated perovskite samples. The 3D map in the bottom row displays the representative uniform distribution of iodine within the perovskite layer for both samples.